

Article

Engineering Band Gap of Ternary $\text{Ag}_2\text{Te}_x\text{S}_{1-x}$ Quantum Dots for Solution-Processed Near-Infrared Photodetectors

Zan Wang^{1,2,3,4} , Yunjiao Gu^{1,2,3}, Daniil Aleksandrov^{1,2,3}, Fenghua Liu^{1,2,3} , Hongbo He^{1,2,3,*} and Weiping Wu^{1,2,3,*} 

¹ Laboratory of Thin Film Optics, Shanghai Institute of Optics and Fine Mechanics, Chinese Academy of Sciences, Shanghai 201800, China

² State Key Laboratory of High Field Laser Physics, Shanghai Institute of Optics and Fine Mechanics, Chinese Academy of Sciences, Shanghai 201800, China

³ University of Chinese Academy of Sciences, Beijing 100049, China

⁴ Department of Optics and Optical Engineering, University of Science and Technology of China, Hefei 230026, China

* Correspondence: hbhe@siom.ac.cn (H.H.); wuwp@siom.ac.cn (W.W.)

Abstract: Silver-based chalcogenide semiconductors exhibit low toxicity and near-infrared optical properties and are therefore extensively employed in the field of solar cells, photodetectors, and biological probes. Here, we report a facile mixture precursor hot-injection colloidal route to prepare $\text{Ag}_2\text{Te}_x\text{S}_{1-x}$ ternary quantum dots (QDs) with tunable photoluminescence (PL) emissions from 950 nm to 1600 nm via alloying band gap engineering. As a proof-of-concept application, the $\text{Ag}_2\text{Te}_x\text{S}_{1-x}$ QDs-based near-infrared photodetector (PD) was fabricated via solution-processes to explore their photoelectric properties. The ICP-OES results reveal the relationship between the compositions of the precursor and the samples, which is consistent with Vegard's equation. Alloying broadened the absorption spectrum and narrowed the band gap of the Ag_2S QDs. The UPS results demonstrate the energy band alignment of the $\text{Ag}_2\text{Te}_{0.53}\text{S}_{0.47}$ QDs. The solution-processed $\text{Ag}_2\text{Te}_x\text{S}_{1-x}$ QD-based PD exhibited a photoresponse to 1350 nm illumination. With an applied voltage of 0.5 V, the specific detectivity is 0.91×10^{10} Jones and the responsivity is 0.48 mA/W. The PD maintained a stable response under multiple optical switching cycles, with a rise time of 2.11 s and a fall time of 1.04 s, which indicate excellent optoelectronic performance.

Keywords: $\text{Ag}_2\text{Te}_x\text{S}_{1-x}$ QDs; ternary alloying; band gap engineering; photodetectors



Citation: Wang, Z.; Gu, Y.; Aleksandrov, D.; Liu, F.; He, H.; Wu, W. Engineering Band Gap of Ternary $\text{Ag}_2\text{Te}_x\text{S}_{1-x}$ Quantum Dots for Solution-Processed Near-Infrared Photodetectors. *Inorganics* **2024**, *12*, 1. <https://doi.org/10.3390/inorganics12010001>

Academic Editor:
Richard Dronskowski

Received: 8 October 2023
Revised: 8 December 2023
Accepted: 11 December 2023
Published: 19 December 2023



Copyright: © 2023 by the authors. Licensee MDPI, Basel, Switzerland. This article is an open access article distributed under the terms and conditions of the Creative Commons Attribution (CC BY) license (<https://creativecommons.org/licenses/by/4.0/>).

1. Introduction

Near-infrared (NIR) light has several advantages, including great penetration depth, strong confidentiality, and excellent anti-electromagnetic interference properties [1–4]. Thus, NIR materials have found extensive applications across diverse domains such as bioimaging, optical communication, photodetectors, and solar cells [5–11]. Currently, NIR materials are mainly concentrated on PbS, PbSe, HgTe QDs, rare-earth nanocrystals, and single-walled carbon nanotubes (SWNTs) [12–16]. Among them, PbS, PbSe, and HgTe QDs contain the toxic heavy metals lead and mercury and rare-earth nanocrystals with non-tunable band gaps and narrow absorption windows. For SWNTs, their application is limited by their broad length distribution, spanning hundreds of nanometers. Therefore, it becomes imperative to foster the creation of novel materials with continuously tunable band gap and high biocompatibility. Silver-based chalcogenide (Ag_2S , Ag_2Se , and Ag_2Te) QDs, as classic NIR materials, possess excellent properties such as low toxicity, wide absorption windows, and good biocompatibility [17–19]. Among these, Ag_2S QDs are one of the most extensively studied semiconductor materials and have ultralow solubility product constants ($K_{\text{sp}}(\text{Ag}_2\text{S}) = 6.69 \times 10^{-50}$), which enable the minimal release of Ag ions in biosystems, thus ensuring their potential application in biomedical, ReRAMs, and

optoelectronic devices [20–22]. However, due to the large band gap of Ag₂S (1.1 eV), its photoluminescence (PL) emission peak is limited to less than 1200 nm, and photodetectors based on this material cannot respond to light in longer wavelength bands and have poor power conversion efficiencies [23]. Therefore, expanding the band gap of Ag₂S and improving its photoelectric performance is very important for the application of Ag₂S materials in the field of optoelectronic devices.

Compared to traditional binary QDs, ternary alloy QDs not only retain the quantum size effect of nanomaterials but also enable effective control of the band gap by adjusting the composition [24,25]. Smith et al. [26] studied the influence of different reactive anion precursors on the size and composition of PbSe_xTe_{1-x}, PbS_xTe_{1-x}, and PbS_xSe_{1-x} QDs. The results demonstrated that the highly reactive Chalcogenide precursors bis(trimethylsilyl) (TMS₂) help to achieve uniform anion incorporation. In addition, it was possible to modulate the excitonic absorption and fluorescence peak of alloy QDs by adjusting the anions ratios. The next generation of electroluminescent displays based on quantum dots requires the development of efficient and stable Cd-free blue emission devices, which remains a challenge due to the poor photophysical properties of blue emission materials. Jang et al. [27] proposed a method by which to synthesize efficient blue-emitting ZnTeSe QDs. They found that the hydrofluoric acid and zinc chloride additives effectively improved the luminescence efficiency by eliminating the layer faults in the ZnSe crystal structure. Moreover, chloride passivation via liquid or solid ligand exchange results in slow radiative recombination, high thermal stability, and efficient charge transport characteristics, and the fluorescence peak was adjusted to 457 nm, while the photoluminescence quantum yield (PLQY) was elevated to a remarkable 100% by controlling the Te doping level. In addition, Ren et al. [28] proposed a water-phase synthesis method for the preparation of NIR CdHgTe alloy quantum dots. CdHgTe QDs are obtained by heating a mixture of CdCl₂, Hg(ClO₄)₂ and NaHTe in the presence of a thiol stabilizer and exhibit PL emission peaks in the range from 600 to 830 nm, which can be adjusted according to size and composition. The PLQY of CdHgTe QDs is about 20–50%, which depends on its emission wavelength and composition. Compared to other reported NIR quantum dots (such as CdTe/CdHgTe and InAs), the prepared CdHgTe alloy quantum dots have a much narrower emission spectrum, with a full width at half-maximum (FWHM) of only 60–80 nm. HRTEM and XRD characterization show that CdHgTe QDs have a good crystal structure and monodispersity. In order to improve the photostability of CdHgTe QDs and reduce their cytotoxicity, CdS nanocrystal shells were added to the surface of CdHgTe QDs. Kim et al. [29] investigated the synthesis of eco-friendly materials AgBiS₂ QDs and the effect of heat treatment on their properties. Increasing the heat treatment temperature reduces the number of surface functional groups, including N (amine) and S (thiol) groups, and there are fewer defects on the particle surface. However, heat treatment at 300 °C reduces PL intensity even when the ligands are fully removed. By measuring the photocurrent response of the AgBiS₂ photodetector to near-infrared light, the photocurrent of the AgBiS₂ photodetector is the highest after heat treatment at 200 °C. Heat treatment removes excessive protective agents and ligands in the inks and improves the photocurrent response of AgBiS₂.

Herein, for the first time, we develop a facile mixture precursor hot-injection method for the synthesis of Ag₂Te_xS_{1-x} alloy QDs. The composition of the alloy QDs was regulated by adjusting the ratio of precursor S to precursor Te. Through augmenting the amount of the precursor Te, the fluorescence peak of the alloy QDs redshifted and the absorption spectrum broadened, thereby achieving controllable tuning of the band gap. Furthermore, a photodetector based on Ag₂Te_{0.53}S_{0.47} QDs as the photosensitive layer has been constructed. The narrow band gap photosensitive layer enables the device to exhibit photoresponse to 1350 nm illumination. The device maintained a stable response and exhibited excellent optoelectronic performance under multiple light switching cycles. This is also the first report on the preparation of Ag₂Te_xS_{1-x} QDs and the investigation of their optoelectronic properties.

2. Experimental Section

2.1. Materials

Silver acetate (AgAc, 99.99%, Alfa Aesar, Haverhill, MA, USA), sulfur powder (S, 99.95%, Aladdin, Shanghai, China), oleylamine (OAm, 80%, Acros, Geel, Belgium), tellurium powder (Te, 99.999%, Alfa Aesar), tri-n-butylphosphine (TBP, >95.0%, TCI, Tokyo, Japan), and 1,2-ethanedithiol (EDT, 98.0%, Alfa Aesar); all these reagents were used without purification.

2.2. Preparation of TBP-Te and TBP-S Precursors

The precursors of TBP-Te and TBP-S were prepared in a glove box. TBP-Te: 2.5 mmol (0.32 g) Te powder was dissolved in 5 mL TBP, employing the use of ultrasonic treatment for a duration of 24 h. TBP-S: 2.5 mmol (0.08 g) S powder was dissolved in 5 mL TBP with vigorous magnetic stirring and ultrasonic treatment for 1 h. The total number of moles of Te and S was kept at 0.10 mmol and the two precursors with different atomic ratios.

2.3. Synthesis of $Ag_2Te_xS_{1-x}$ QDs

In the conventional hot-injection method, a blend comprising AgAc (0.067 g, 0.4 mmol) and Oam (16 mL) was introduced into a 100 mL three-neck flask at room temperature. Subsequently, the solution underwent a remove oxygen process through vigorous magnetic stirring while maintaining a vacuum for 30 min. Afterwards, the temperature of the reaction was subsequently elevated to 120 °C in the presence of a nitrogen atmosphere, resulting in the attainment of a transparent solution. Then, 0.2 mL mixture precursor (TBP-S and TBP-Te) was injected into the solution while vigorously stirring at a speed of 1000 rpm. This temperature was maintained for a duration of 5 min to ensure the consistent growth of the QDs. The products were precipitated with ethanol and recovered by centrifugation at a speed of 12,000 rpm for 10 min. The products were dispersed in chloroform (15 mg/mL). A series of $Ag_2Te_xS_{1-x}$ samples were used, referred to as S/Te-A (S:Te = 1:0), S/Te-B (S:Te = 2:1), S/Te-C (S:Te = 1:1), and S/Te-D (S:Te = 0:1).

2.4. Photodetector Fabrication

The photodetector device fabrication and ligand exchange protocol is based on previous research [30]. At first, this process begins with cleaning the glass substrates. Then the $Ag_2Te_xS_{1-x}$ QDs solution was deposited onto the glass substrate by employing the spin-coating technique under a speed of 1500 rpm and kept for 30 s. Subsequently, a volume of 500 μ L of ligand solution (consisting of 5 mM EDT dissolved in acetonitrile) was gently applied onto the film for a duration of 30 s, followed by removal of the ligand solution using a spinning method. Afterwards, the QD film was immersed in acetonitrile 3 times to eliminate any remaining unbound ligands. The ligand exchange and spin-coating were iterated 6 times. Finally, 5 nm/100 nm-thick Ti/Au metal electrodes were deposited through an interdigitated shadow mask (the channel width is 50 μ m and the size is 18 mm \times 18 mm) through a thermal evaporator.

2.5. Characterizations

Talos F200X (ThermoFisher, Waltham, MA, USA) was used to test transmission electron microscope (TEM) and high-resolution TEM (HRTEM) images of $Ag_2Te_xS_{1-x}$ QDs under an acceleration voltage of 200 kV. X-ray diffraction (XRD) patterns were measured by a PANalytical Empyrean diffractometer (Malven PANalytical, Almelo, Holland) (Cu-K α λ = 1.54056 Å) in the range of 20–80°. An inductively coupled plasma optical emission spectrometer (ICP-OES) was performed on PerkinElmer Avio 500 (PerkinElmer, Waltham, MA, USA). The absorption spectra were recorded with a PerkinElmer Lambda 750 spectrometer (PerkinElmer, Waltham, MA, USA). The NIR fluorescence spectra were executed on an Applied NanoFluorescence Spectrometer (Houston, TX, USA), applying an excitation laser source of 785 nm. The X-ray photoelectron spectroscopy (XPS) were collected on a PHI-5000 VersaProbe instrument (ULVAC-PHI, Chigasaki, Japan) using Al/K α radiation as excitation source, the electron emission angle is 34°, the diameter of

the X-ray spot is 250 μm , the base pressure is 4.17×10^{-7} mBar during the analyses, the samples are etched for 60 s with 1 keV Ar^+ ions before the XPS scan to remove the surface layer which adsorb water and oxygen in the air. All the XPS spectra recorded for Ag 3d, Te 3d, and S 2p were referenced to the C 1s peak, which was calibrated by positioning it to 289.58 eV $-\Phi$. The 289.58 eV is the binding energy position of the C 1s peak with respect to the vacuum level, and Φ is the work function of $\text{Ag}_2\text{Te}_{0.53}\text{S}_{0.47}$ (~ 5.16 eV) [31,32]. Thus, the set value of the extraneous polluted carbon is 284.42 eV. The ultraviolet photoelectron spectroscopy (UPS) was measured by using a Thermo ESCALAB 250Xi instrument (ThermoFisher, Waltham, MA, USA) with He I radiation. The Keithley 4200-SCS semiconductor analyzer equipped with a Signatone S-1160 Probe Station (Signatone, Gilroy, CA, USA) is employed to characterize the optoelectronic performance of devices.

3. Results and Discussion

Figure 1 displays the low-magnification TEM and HRTEM images of $\text{Ag}_2\text{Te}_x\text{S}_{1-x}$ QDs, which exhibit excellent dispersibility, clear lattice patterns, and good crystallinity. Figure 1a shows TEM image of Ag_2S QDs (denoted as S/Te-A), which appear as uniformly spherical particles. With the increase in the Te content, the morphology of the QDs gradually transformed from uniform spherical morphology to a branch-like structure, as shown in Figure 1b,c (denoted as S/Te-B and S/Te-C, respectively). When all the S elements are replaced by Te, the morphology changes to a branch-like structure composed of interconnected spherical particles (S/Te-D), as depicted in Figure 1d.

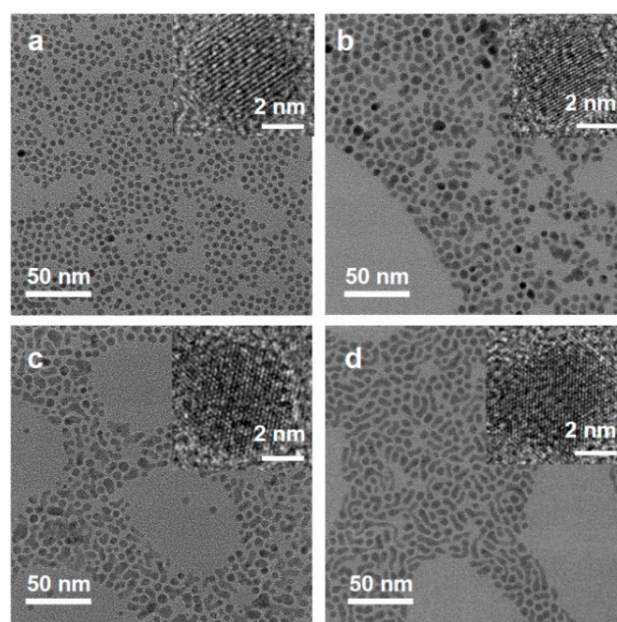


Figure 1. TEM and HRTEM images of $\text{Ag}_2\text{Te}_x\text{S}_{1-x}$ QDs: (a) S/Te-A, (b) S/Te-B, (c) S/Te-C, and (d) S/Te-D.

Similar results have been reported in other studies on Ag_2Te QDs, which elucidate that this morphology is mainly attributed to the driving force generated by strong dipole-dipole interactions, leading to the formation of a branch-like structure [33]. Additionally, we performed a statistical analysis of the size distributions of the different $\text{Ag}_2\text{Te}_x\text{S}_{1-x}$ QDs (100 particles counted in each image, Figure S1). The diameters of S/Te-A, S/Te-B, S/Te-C, and S/Te-D were measured as 3.92 ± 0.19 nm, 5.45 ± 0.31 nm, 5.32 ± 0.51 nm, and 5.23 ± 0.32 nm, respectively.

To investigate the crystal structure of the $\text{Ag}_2\text{Te}_x\text{S}_{1-x}$ QDs, we measured the XRD patterns of the samples with different S/Te ratios. Figure 2 shows the S/Te-A sample consisting of Ag_2S QDs, with diffraction peaks matching those of Ag_2S crystals (JCPDS:14-0072) and exhibiting a relatively broad peak width, which is attributed to the small size of the QDs.

The characteristic diffraction peaks of Ag_2S in the $\text{Ag}_2\text{Te}_x\text{S}_{1-x}$ QDs gradually weakened with increasing Te content, indicating a phase transition from monoclinic Ag_2S crystals (JCPDS:14-0072) to monoclinic Ag_2Te crystals (JCPDS:81-1820). Finally, the characteristic diffraction peaks of the S/Te-D sample coincided with those of pure Ag_2Te crystals (JCPDS:81-1820), exhibiting broadened diffraction peaks. ICP-OES was used to analyze the actual atomic ratios of the S and Te anions in the samples. Figure S2 illustrates the relationship between $\text{Te}/(\text{Te} + \text{S})$ for the precursors and the products of the four samples. When the molar ratio of the Te source to the S source is 1:2, the Te-to-S ratio in the product is 0.54:1 ($\text{Ag}_2\text{Te}_{0.35}\text{S}_{0.65}$). When the molar ratio of the Te source to the S source turns to 1:1, the Te-to-S ratio in the product becomes 1.13:1 ($\text{Ag}_2\text{Te}_{0.53}\text{S}_{0.47}$) owing to the slightly higher reactivity of the Te source compared to that of the S source. These results demonstrate that the manipulation of the anion ratio in the precursor mixture is an effective means of controlling the anion content within the alloy QDs.

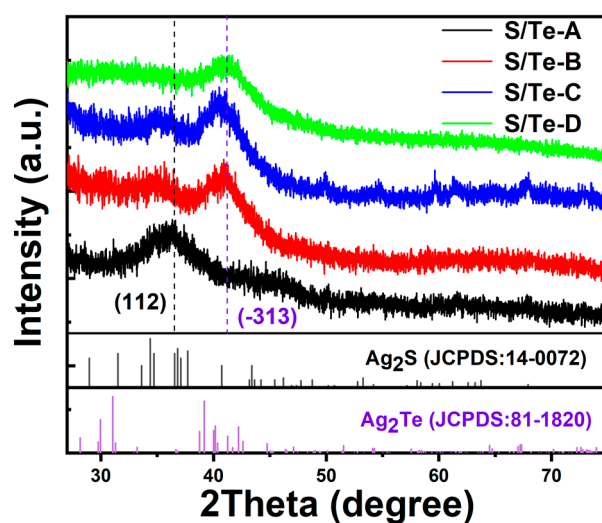


Figure 2. XRD patterns of four different $\text{Ag}_2\text{Te}_x\text{S}_{1-x}$ QDs.

XPS was used to characterize the elements and their valence states in the alloyed QDs. Figure 3a shows the low-resolution scan spectrum of the $\text{Ag}_2\text{Te}_{0.53}\text{S}_{0.47}$ QDs, which demonstrates the sample contains Ag, Te, O, S, and C elements. Figure 3b–d show the high-resolution scan spectra of Ag 3d, Te 3d, and S 2p. As illustrated in Figure 3b, the high-resolution Ag 3d region spectra of $\text{Ag}_2\text{Te}_{0.53}\text{S}_{0.47}$ QDs show two symmetric peaks, Ag 3d_{5/2} and Ag 3d_{3/2}, which correspond to binding energies of 367.7 eV and 373.7 eV, respectively. This confirms that the oxidation state of silver is univalent (Ag^+) [34]. In Figure 3c, the high-resolution Te 3d region spectra show two peaks, Te 3d_{5/2} and Te 3d_{3/2}, which correspond to binding energies of 572.0 eV and 582.4 eV, respectively, suggesting that the valence of telluride is negative bivalence (Te^{2-}) [35,36]. Furthermore, the spectrum of the S 2p region was characterized and analysed (Figure 3d). The spectrum contains multiple peaks, which must be separated. Fitting the low-binding-energy peaks yields two distinct peaks with binding energies measuring 162.6 eV and 161.3 eV. These peaks can be attributed to the S 2p_{1/2} and S 2p_{3/2}, respectively, in agreement with the Ag-S binding energies [37]. An additional peak appears in the high-energy region (approximately 168.3 eV), indicating that a small fraction of S may have undergone oxidation to form sulfate ions upon exposure to air [38].

Figure 4 shows the PL emission spectra of $\text{Ag}_2\text{Te}_x\text{S}_{1-x}$ QDs with four different S/Te ratios under 785 nm excitation. The dashed lines represent the spectral regions that could not be detected because of the response range of the spectrometer (900 nm–1700 nm). The fluorescence peak of the $\text{Ag}_2\text{Te}_x\text{S}_{1-x}$ QDs exhibits a gradual redshift, transitioning from 955 nm to 1255 nm, 1470 nm, and ultimately reaching 1605 nm. When the size of the direct band gap semiconductor decreases, the PL emission should blue-shift. However,

the size of $\text{Ag}_2\text{Te}_x\text{S}_{1-x}$ QDs decreases, and the PL peak redshift contradicts the above theory (S/Te-B to S/Te-D). This anomalous phenomenon can be explained by Vegard's law, which describes the relationship between the band gap of ternary alloy materials and their elemental composition of elements [39]. The band gap of $\text{Ag}_2\text{Te}_x\text{S}_{1-x}$ alloy can be described as follows:

$$E_{\text{alloy}} = xE_t + (1 - x)E_s \quad (1)$$

where x is the proportion of component t ; and E_{alloy} , E_t , and E_s are the band gap energies of the alloy material, pure t , and pure s , respectively. Because the band gap of Ag_2Te (0.06 eV) [40] is much smaller than that of Ag_2S (1.1 eV) [41], as the Te content increases, the value of x increases, leading to a decrease in the band gap of the alloy QDs and a redshift in the PL emission peaks.

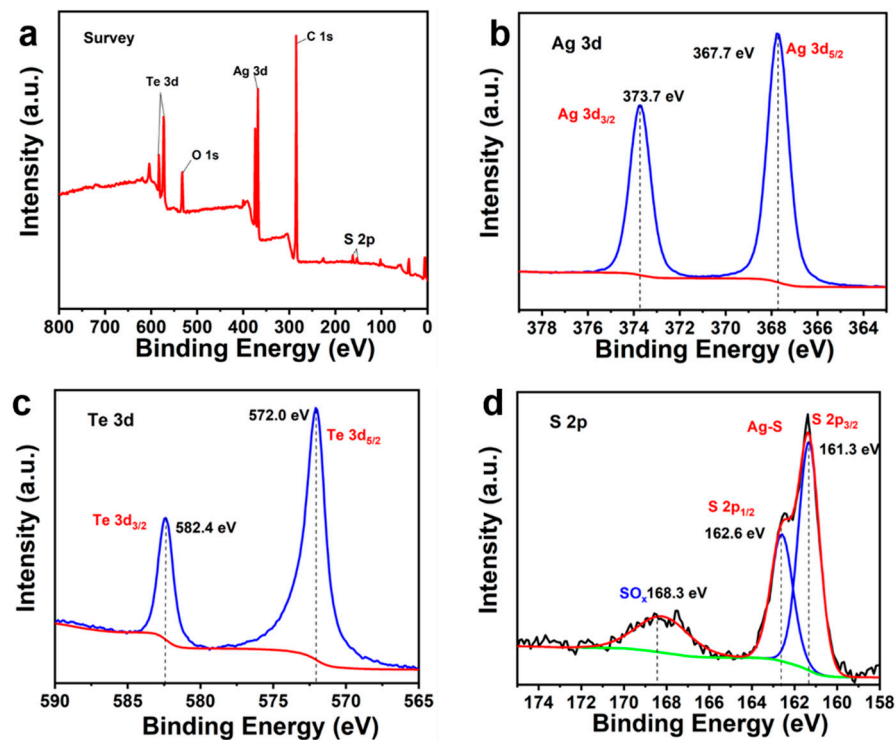


Figure 3. (a) Survey XPS spectra of $\text{Ag}_2\text{Te}_x\text{S}_{1-x}$ QDs. High-resolution XPS spectra for (b) Ag 3d, (c) Te 3d, and (d) S 2p. The overlapped spectra of S were fitted with the Gaussian function.

Figure 5 shows the absorption spectra of $\text{Ag}_2\text{Te}_x\text{S}_{1-x}$ QDs with four different S/Te ratios. The S/Te-A to S/Te-D samples do not exhibit distinct excitonic absorption peaks, which is similar to previous reports of Ag_2S QDs and Ag_2Te QDs [42,43]. The optical band gap values of $\text{Ag}_2\text{Te}_x\text{S}_{1-x}$ QDs are calculated by the extrapolated energy intercept of the Tauc plot. For direct bandgap materials, the Tauc equation can be described as follows [44]:

$$\alpha h\nu = A(h\nu - E_g)^{1/2} \quad (2)$$

where α is the absorption coefficient; $h\nu$ is the incident photon energy; A is a proportionality constant; and E_g is the optical band gap, respectively. The band gap was calculated to be 1.45 eV, 1.07 eV, 0.89 eV, and 0.84 eV for S/Te-A, S/Te-B, S/Te-C, and S/Te-D, respectively. As the Te content increased, the absorption wavelength ranges of the alloy QDs broadened, and the band gap decreased. This result is consistent with the alterations observed in the PL emission spectra of $\text{Ag}_2\text{Te}_x\text{S}_{1-x}$ QDs. Furthermore, the result reveals that the adjustment of Te content effectively controls the band gap of $\text{Ag}_2\text{Te}_x\text{S}_{1-x}$ QDs.

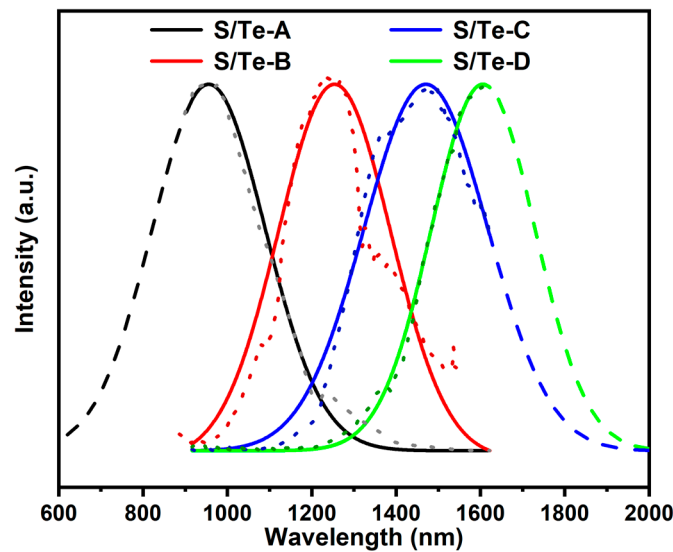


Figure 4. PL emission spectra of the obtained four different $\text{Ag}_2\text{Te}_x\text{S}_{1-x}$ QDs under an excitation of 785 nm (the dotted lines are the real raw experimental data, and the solid lines are the corresponding Gaussian fitting data).

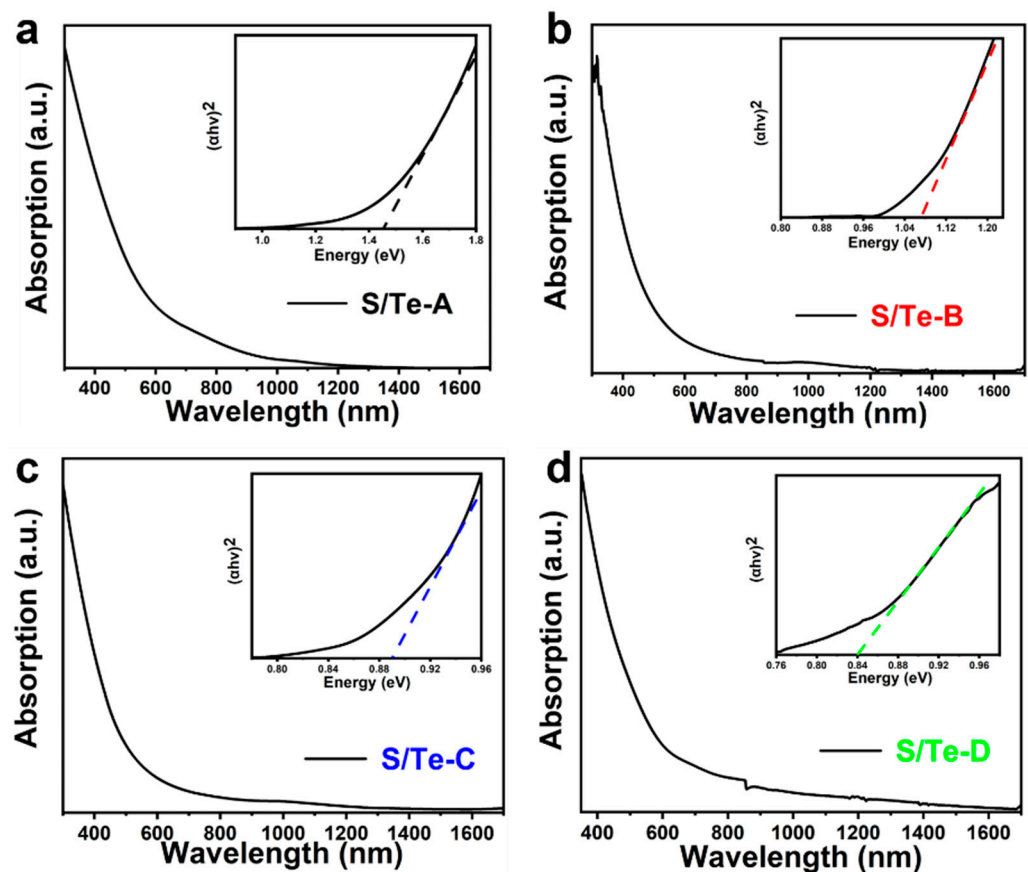


Figure 5. Absorption spectrum and Tauc plot for estimating E_g (insert) of four different $\text{Ag}_2\text{Te}_x\text{S}_{1-x}$ samples: (a) S/Te-A, (b) S/Te-B, (c) S/Te-C, and (d) S/Te-D.

UPS was used to measure the kinetic energy of the $\text{Ag}_2\text{Te}_{0.53}\text{S}_{0.47}$ QDs, as shown in Figure 6. The test sample was prepared by spin-coating it into a thin film on a glass substrate. Figure 6a shows the survey of UPS spectrum of the $\text{Ag}_2\text{Te}_{0.53}\text{S}_{0.47}$ QDs. Figure 6b portrays the region of high binding energy cutoff. The tangent value in the cutoff region is approximately 16.6 eV, indicating that the Fermi level positioning of the alloy QDs is

4.61 eV. Combined with the low binding energy cutoff region shown in Figure 6c (with a tangent value of approximately 0.54 eV), the energy level of the valence band maximum (E_{VB}) was calculated to be 5.15 eV (relative to the vacuum level E_{Vac}). Finally, combined with the band gap of $Ag_2Te_{0.53}S_{0.47}$ QDs ($E_g = 0.89$ eV), the energy level of the conduction band minimum (E_{CB}) can be calculated to be 4.26 eV. Therefore, the accurate depiction of the energy band alignment for the $Ag_2Te_{0.53}S_{0.47}$ QDs is depicted in Figure S3.

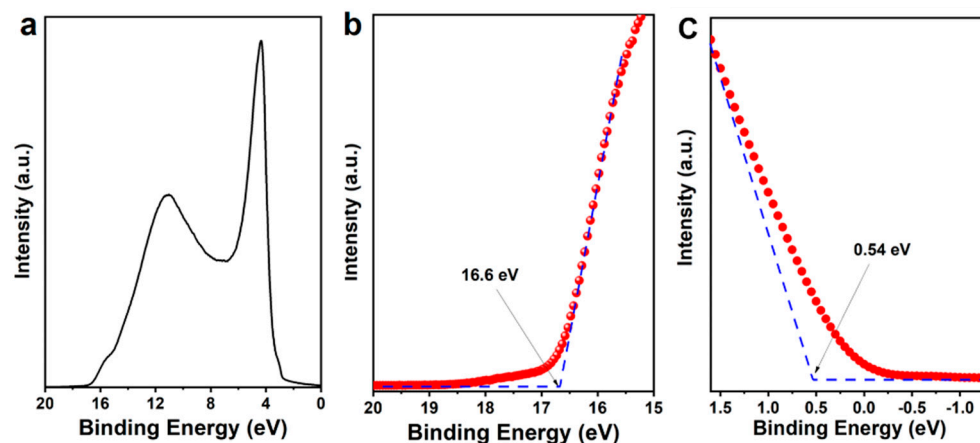


Figure 6. (a) Survey UPS spectrum of the $Ag_2Te_{0.53}S_{0.47}$ QDs. Amplified areas of (b) the high binding energy regions and (c) the low binding energy regions.

As a proof-of-concept application, $Ag_2Te_xS_{1-x}$ QDs were used as the active layer for the photodetector (PD) device. The photoelectric properties of $Ag_2Te_xS_{1-x}$ QD-based PD were investigated (Figure S4). Figure S4a,b show that neither the Ag_2S QD-based or $Ag_2Te_{0.53}S_{0.47}$ QD-based PD have any response to 1350 nm illumination. This can be attributed to the large band gap of these two QDs, which cannot be excited by 1350 nm light to generate photocurrent. With the increase in Te component, both $Ag_2Te_{0.53}S_{0.47}$ QD-based and Ag_2Te QD-based PD generate photocurrent under 1350 nm illumination, and the light response of $Ag_2Te_{0.53}S_{0.47}$ QDs is more obvious than that of Ag_2Te QDs. Thus, composition adjustment can not only expand the band gap of QDs, but also help to improve the performance of photodetectors.

In order to evaluate the performance of $Ag_2Te_xS_{1-x}$ QD-based PDs, the corresponding figures of merit were calculated. The two representative parameters (responsivity R and special detectivity D^*) were determined as follows [45]:

$$R = \frac{I_{ph} - I_d}{P} \quad (3)$$

$$D^* = \frac{A^{1/2} \cdot R}{(2q \cdot I_d)^{1/2}} \quad (4)$$

where I_{ph} is the photocurrent; I_d is the dark current; P is the radiated power (product of active area and incident light density); A is the active area of the photodetector; and q is the electron charge. At an applied voltage of 0.5 V and an illumination intensity of 2 mW/cm², the D^* of the $Ag_2Te_{0.53}S_{0.47}$ QD-based PD reaches 0.91×10^{10} Jones, and the R is 0.48 mA/W. In addition, the response speed of the $Ag_2Te_{0.53}S_{0.47}$ QD-based PD was determined using the rise time (τ_r) and fall time (τ_f). Figure 7 shows the response speed curve of the detector at a bias voltage of 0.5 V and an illumination intensity of 2 mW/cm². Figure 7a shows the detector still exhibits good repeatability under continuous 10-cycle switching. The fluctuations observed in the light and dark states may be caused by surface defects generated from ligand exchange processes. Figure 7b demonstrates that τ_r was 2.11 s and τ_f was 1.04 s within one switching cycle.

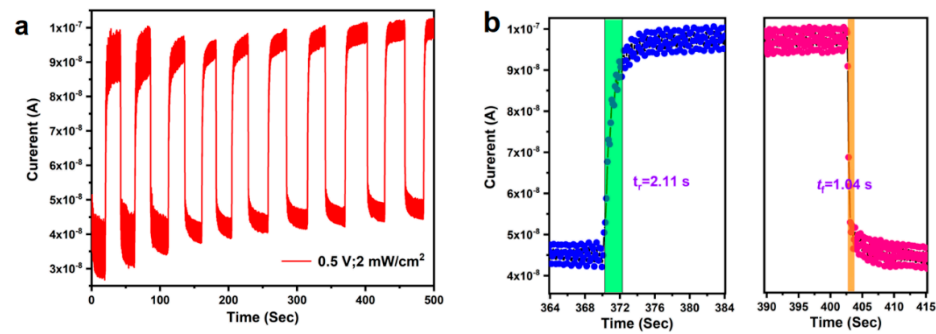


Figure 7. (a) Time response of $\text{Ag}_2\text{Te}_{0.53}\text{S}_{0.47}$ QD-based PD at 0.5 V under 1350 nm NIR illumination with power densities of 2 mW/cm^2 . (b) I–t curve for determining the rise and fall time of $\text{Ag}_2\text{Te}_{0.53}\text{S}_{0.47}$ QD-based PD.

In order to elucidate the electron–hole transport mechanism in the photodetector, the schematic of energy band diagrams of $\text{Au}/\text{Ag}_2\text{Te}_x\text{S}_{1-x}$ QDs/ Au PD on the glass substrate is shown in Figure 8. Figure 8a shows the energy band diagram of the $\text{Ag}_2\text{Te}_x\text{S}_{1-x}$ QD-based PD under dark and without external bias. The contact between the metal electrode (Au) and $\text{Ag}_2\text{Te}_x\text{S}_{1-x}$ QDs exhibits a slight barrier height (Φ_{SBH}), which proves that the contact between Au and the $\text{Ag}_2\text{Te}_x\text{S}_{1-x}$ QDs is not a simple Ohmic contact but a Schottky contact. This is consistent with the results of the nonlinear I–V curve of the $\text{Ag}_2\text{Te}_x\text{S}_{1-x}$ QD-based PD. Figure 8b shows the energy band diagram of the $\text{Ag}_2\text{Te}_x\text{S}_{1-x}$ QD-based PD under NIR light with a wavelength of 1350 nm illumination and without external bias. The $\text{Ag}_2\text{Te}_x\text{S}_{1-x}$ QDs are excited to produce charge carriers (electron–hole pairs), which are transported between the $\text{Ag}_2\text{Te}_x\text{S}_{1-x}$ QDs due to the quantum tunneling effect. However, only a very small number of carriers can reach the electrode due to the influence of the Schottky barrier. Therefore, no photocurrent can be observed. In addition, under illumination and with external bias, the trap states of $\text{Ag}_2\text{Te}_x\text{S}_{1-x}$ QDs (including surface defect levels and internal defect levels) serve as trapping centers for photogenerated holes [46]. This results in a reduction in the depletion region width and Φ_{SBH} , which offers favorable conditions for carriers tunneling from the $\text{Ag}_2\text{Te}_x\text{S}_{1-x}$ QDs to the metal electrode under external bias, causing increased photocurrent (Figure 8c).

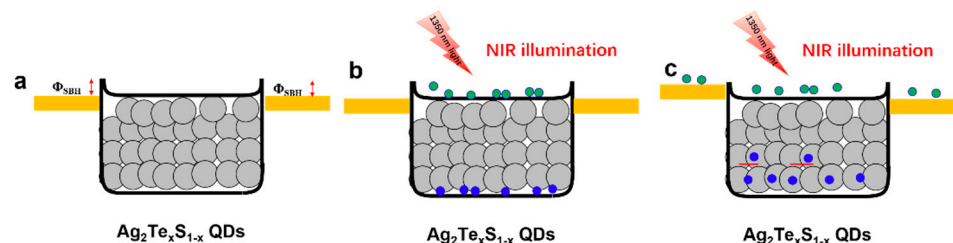


Figure 8. The schematic of energy band diagrams of $\text{Au}/\text{Ag}_2\text{Te}_x\text{S}_{1-x}$ QDs/ Au PD on the glass substrate: (a) under dark and without external bias; (b) under NIR light with a wavelength of 1350 nm illumination and without external bias; (c) under illumination and with external bias.

4. Conclusions

In summary, we have successfully prepared $\text{Ag}_2\text{Te}_x\text{S}_{1-x}$ ternary QDs via a facile mixture precursor hot-injection method. TEM images and XRD confirmed that the morphology and lattice parameter gradually shifted from Ag_2S to $\text{Ag}_2\text{Te}_x\text{S}_{1-x}$ and finally to Ag_2Te QDs. The ICP-OES results reveal the relationship between the compositions of the precursor and samples, which is consistent with Vegard’s equation. In addition, optical characterization confirms the feasibility of $\text{Ag}_2\text{Te}_x\text{S}_{1-x}$ QDs with tunable PL emission and band gap by alloying engineering. The E_{VB} and E_{CB} values of the $\text{Ag}_2\text{Te}_{0.53}\text{S}_{0.47}$ QDs were also calculated using UPS and absorption spectra, and an accurate diagram of the energy band alignment was plotted. The $\text{Ag}_2\text{Te}_x\text{S}_{1-x}$ QD-based PD was fabricated to investigate

their photoelectric properties. The PD shows good photoresponse at 1350 nm illumination, D^* is 0.91×10^{10} Jones, and R is 0.48 mA/W under an applied voltage of 0.5 V and power densities of 2 mW/cm². The PD maintains a stable response under multiple optical switching cycles, with a rise time of 2.11 s and a fall time of 1.04 s, indicating excellent optoelectronic performance. Therefore, the novel Ag₂Te_xS_{1-x} ternary alloy QDs extend the photoresponse range of Ag₂S QDs, demonstrating promising potential in near-infrared PL emission and photodetection.

Supplementary Materials: The following supporting information can be downloaded at <https://www.mdpi.com/article/10.3390/inorganics12010001/s1>: Figure S1: The size distribution of Ag₂Te_xS_{1-x} QDs; Figure S2: ICP-OES data shows the relative amount of Te in the product versus the relative amount of Te in the precursor solution. Figure S3: The schematic band alignment of Ag₂Te_{0.53}S_{0.47} alloyed QDs. Figure S4: The I-V characteristics of the fabricated Ag₂Te_{0.53}S_{0.47} QD-based PD in dark and under 1350 nm NIR light with power densities of 2 mW/cm².

Author Contributions: Conceptualization, Z.W., H.H. and W.W.; methodology, Z.W.; formal analysis, Z.W.; investigation, Z.W., D.A. and W.W.; re-sources, H.H. and W.W.; data curation, Z.W.; writing—original draft preparation, Z.W.; writing—review and editing, Y.G., D.A., F.L. and W.W.; visualization, Z.W. and D.A.; supervision, H.H. and W.W.; project administration, Y.G., F.L., H.H. and W.W.; funding acquisition, Y.G., F.L., H.H. and W.W. All authors have read and agreed to the published version of the manuscript.

Funding: This work is supported by the National Natural Science Foundation of China (No. 52273242, No. 61975219, No. 22202231), the National Key R&D Program of China (No. 2021YFB2800703, No. 2021YFB2800701) and the Chinese Academy of Sciences.

Data Availability Statement: The data presented in this study are available in article.

Conflicts of Interest: The authors declare no conflict of interest.

References

1. Aiello, R.; Di Sarno, V.; Santi, M.G.D.; De Rosa, M.; Ricciardi, I.; Giusfredi, G.; De Natale, P.; Santamaria, L.; Maddaloni, P. Lamb-dip saturated-absorption cavity ring-down rovibrational molecular spectroscopy in the near-infrared. *Photonics Res.* **2022**, *10*, 1803–1809. [[CrossRef](#)]
2. Shanmugam, V.; Selvakumar, S.; Yeh, C.S. Near-infrared light-responsive nanomaterials in cancer therapeutics. *Chem. Soc. Rev.* **2014**, *43*, 6254–6287. [[CrossRef](#)]
3. Zhang, Q.Q.; Li, Y.; Jiang, C.H.; Sun, W.B.; Tao, J.W.; Lu, L.H. Near-infrared light-enhanced generation of hydroxyl radical for cancer immunotherapy. *Adv. Healthc. Mater.* **2023**, *12*, 2301502. [[CrossRef](#)]
4. Sun, P.; Zhang, M.D.; Dong, F.L.; Feng, L.F.; Chu, W.G. Broadband achromatic polarization insensitive metalens over 950 nm bandwidth in the visible and near-infrared. *Chin. Opt. Lett.* **2022**, *20*, 013601. [[CrossRef](#)]
5. Tan, L.L.; Fu, Y.Q.; Kang, S.L.; Wondraczek, L.; Lin, C.G.; Yue, Y.Z. Broadband NIR-emitting Te cluster-doped glass for smart light source towards night-vision and NIR spectroscopy applications. *Photonics Res.* **2022**, *10*, 1187–1193. [[CrossRef](#)]
6. Wang, Y.H.; Bai, S.C.; Sun, J.; Liang, H.; Li, C.; Tan, T.Y.; Yang, G.; Wang, J.W. Highly efficient visible and near-infrared luminescence of Sb³⁺, Tm³⁺ co-doped Cs₂NaYCl₆ lead-free double perovskite and light emitting diodes. *J. Alloys Compd.* **2023**, *947*, 169602. [[CrossRef](#)]
7. Kufer, D.; Nikitskiy, I.; Lasanta, T.; Navickaite, G.; Koppens, F.H.L.; Konstantatos, G. Hybrid 2D-0D MoS₂-PbS quantum dot photodetectors. *Adv. Mater.* **2015**, *27*, 176–180. [[CrossRef](#)]
8. Zhang, H.; Kumar, S.; Sua, Y.M.; Zhu, S.Y.; Huang, Y.P. Near-infrared 3D imaging with upconversion detection. *Photonics Res.* **2022**, *10*, 2760–2767. [[CrossRef](#)]
9. Zeng, X.K.; Wang, C.Y.; Cai, Y.; Lin, Q.G.; Lu, X.W.; Lin, J.H.; Yuan, X.M.; Cao, W.H.; Ai, Y.X.; Xu, S.X. High spatial-resolution biological tissue imaging in the second near-infrared region via optical parametric amplification pumped by an ultrafast vortex pulse. *Chin. Opt. Lett.* **2022**, *20*, 100003. [[CrossRef](#)]
10. Konstantatos, G.; Badioli, M.; Gaudreau, L.; Osmond, J.; Bernechea, M.; Garcia de Arquer, F.P.; Gatti, F.; Koppens, F.H.L. Hybrid graphene-quantum dot phototransistors with ultrahigh gain. *Nat. Nanotechnol.* **2012**, *7*, 363–368. [[CrossRef](#)]
11. Koppens, F.H.L.; Mueller, T.; Avouris, P.; Ferrari, A.C.; Vitiello, M.S.; Polini, M. Photodetectors based on graphene, other two-dimensional materials and hybrid systems. *Nat. Nanotechnol.* **2014**, *9*, 780–793. [[CrossRef](#)]
12. Wang, Z.; Li, J.B.; Huang, F.F.; Hua, Y.J.; Tian, Y.; Zhang, X.H.; Xu, S.Q. Multifunctional optical materials based on transparent inorganic glasses embedded with PbS QDs. *J. Alloys Compd.* **2023**, *942*, 169040. [[CrossRef](#)]
13. Semonin, O.E.; Luther, J.M.; Choi, S.; Chen, H.Y.; Gao, J.B.; Nozik, A.J.; Beard, M.C. Peak external photocurrent quantum efficiency exceeding 100% via MEG in a quantum dot solar cell. *Science* **2011**, *334*, 1530–1533. [[CrossRef](#)] [[PubMed](#)]

14. Chen, M.Y.; Lu, H.P.; Abdelazim, N.M.; Zhu, Y.; Wang, Z.; Ren, W.; Kershaw, S.V.; Rogach, A.L.; Zhao, N. Mercury telluride quantum dot based phototransistor enabling high-sensitivity room-temperature photodetection at 2000 nm. *ACS Nano* **2017**, *11*, 5614–5622. [[CrossRef](#)]
15. Wang, R.; Li, X.M.; Zhou, L.; Zhang, F. Epitaxial seeded growth of rare-earth nanocrystals with efficient 800 nm near-infrared to 1525 nm short-wavelength infrared downconversion photoluminescence for in vivo bioimaging. *Angew. Chem. Int. Ed.* **2014**, *53*, 12086–12090. [[CrossRef](#)]
16. Kong, J.; Franklin, N.R.; Zhou, C.W.; Chapline, M.G.; Peng, S.; Cho, K.J.; Dai, H.J. Nanotube molecular wires as chemical sensors. *Science* **2000**, *287*, 622–625. [[CrossRef](#)]
17. Dong, B.H.; Li, C.Y.; Chen, G.C.; Zhang, Y.J.; Zhang, Y.; Deng, M.J.; Wang, Q.B. Facile synthesis of highly photoluminescent Ag₂Se quantum dots as a new fluorescent probe in the second near-infrared window for in vivo imaging. *Chem. Mater.* **2013**, *25*, 2503–2509. [[CrossRef](#)]
18. Gu, Y.P.; Cui, R.; Zhang, Z.L.; Xie, Z.X.; Pang, D.W. Ultrasmall near-infrared Ag₂Se quantum dots with tunable fluorescence for in vivo imaging. *J. Am. Chem. Soc.* **2012**, *134*, 79–82. [[CrossRef](#)]
19. Li, C.Y.; Zhang, Y.J.; Wang, M.; Zhang, Y.; Chen, G.C.; Li, L.; Wu, D.M.; Wang, Q.B. In vivo real-time visualization of tissue blood flow and angiogenesis using Ag₂S quantum dots in the NIR-II window. *Biomaterials* **2014**, *35*, 393–400. [[CrossRef](#)]
20. Zhao, C.; Chen, C.L.; Wei, R.; Zou, Y.T.; Kong, W.C.; Huang, T.; Yu, Z.; Yang, J.J.; Li, F.; Han, Y.; et al. Laser-assisted synthesis of Ag₂S-quantum-dot-in-perovskite matrix and its application in broadband photodetectors. *Adv. Opt. Mater.* **2022**, *10*, 2101535. [[CrossRef](#)]
21. Martin-Garcia, B.; Spirito, D.; Krahn, R.; Moreels, I. Solution-processed silver sulphide nanocrystal film for resistive switching memories. *J. Mater. Chem. C* **2018**, *6*, 13128–13135. [[CrossRef](#)]
22. Wang, B.; Zhao, C.; Lu, H.Y.; Zou, T.T.; Singh, S.C.; Yu, Z.; Yao, C.M.; Zheng, X.; Xing, J.; Zou, Y.T.; et al. SERS study on the synergistic effects of electric field enhancement and charge transfer in an Ag₂S quantum dots/plasmonic bowtie nanoantenna composite system. *Photonics Res.* **2020**, *8*, 548–563. [[CrossRef](#)]
23. Zhang, Y.; Hong, G.S.; Zhang, Y.J.; Chen, G.C.; Li, F.; Dai, H.J.; Wang, Q.B. Ag₂S quantum dot: A bright and biocompatible fluorescent nanoprobe in the second near-infrared window. *ACS Nano* **2012**, *6*, 3695–3702. [[CrossRef](#)]
24. Ji, C.Y.; Zhang, Y.; Zhang, X.Y.; Wang, P.; Shen, H.Z.; Gao, W.Z.; Wang, Y.D.; Yu, W.W. Synthesis and characterization of Ag₂S_xSe_{1-x} nanocrystals and their photoelectrochemical property. *Nanotechnology* **2017**, *28*, 065602. [[CrossRef](#)] [[PubMed](#)]
25. Bailey, R.E.; Nie, S.M. Alloyed semiconductor quantum dots: Tuning the optical properties without changing the particle size. *J. Am. Chem. Soc.* **2003**, *125*, 7100–7106. [[CrossRef](#)] [[PubMed](#)]
26. Smith, D.K.; Luther, J.M.; Semonin, O.E.; Nozik, A.J.; Beard, M.C. Tuning the synthesis of ternary lead chalcogenide quantum dots by balancing precursor reactivity. *ACS Nano* **2011**, *5*, 183–190. [[CrossRef](#)]
27. Kim, T.; Kim, K.H.; Kim, S.; Choi, S.M.; Jang, H.; Seo, H.K.; Lee, H.; Chung, D.Y.; Jang, E. Efficient and stable blue quantum dot light-emitting diode. *Nature* **2020**, *586*, 385–389. [[CrossRef](#)]
28. Qian, H.; Dong, C.; Peng, J.; Qiu, X.; Xu, Y.; Ren, J. High-quality and water-soluble near-infrared photoluminescent CdHgTe/CdS quantum dots prepared by adjusting size and composition. *J. Phys. Chem. C* **2007**, *111*, 16852–16857. [[CrossRef](#)]
29. Nakazawa, T.; Kim, D.; Oshima, Y.; Sato, H.; Park, J.; Kim, H. Synthesis and application of AgBiS₂ and Ag₂S nanoinks for the production of IR photodetectors. *ACS Omega* **2021**, *6*, 20710–20718. [[CrossRef](#)]
30. Grotevent, M.J.; Hail, C.U.; Yakunin, S.; Bachmann, D.; Kara, G.; Dirin, D.N.; Calame, M.; Poulikakos, D.; Kovalenko, M.V.; Shorubalko, I. Temperature-dependent charge carrier transfer in colloidal quantum dot/graphene infrared photodetectors. *ACS Appl. Mater. Interfaces* **2021**, *13*, 848–856. [[CrossRef](#)]
31. Bhatt, V.; Kumar, M.; Kim, E.C.; Chung, H.J.; Yun, J.H. Wafer-scale, thickness-controlled p-CuInSe₂/n-Si heterojunction for self-biased, highly sensitive, and broadband photodetectors. *ACS Appl. Electron.* **2022**, *4*, 6284–6299. [[CrossRef](#)]
32. Hu, H.; Wu, C.; He, C.; Shen, J.; Cheng, Y.; Wu, F.; Wang, S.; Guo, D. Improved photoelectric performance with self-powered characteristics through TiO₂ surface passivation in an α-Ga₂O₃ nanorod array deep ultraviolet photodetector. *ACS Appl. Electron. Mater.* **2022**, *4*, 3801–3806. [[CrossRef](#)]
33. Zhang, Y.J.; Yang, H.C.; An, X.Y.; Wang, Z.; Yang, X.H.; Yu, M.X.; Zhang, R.; Sun, Z.Q.; Wang, Q.B. Controlled synthesis of Ag₂Te@Ag₂S core-shell quantum dots with enhanced and tunable fluorescence in the second near-infrared window. *Small* **2020**, *16*, 2001003. [[CrossRef](#)]
34. Wang, Z.; Liu, F.H.; Gu, Y.J.; Hu, Y.G.; Wu, W.P. Solution-processed self-powered near-infrared photodetectors of toxic heavy metal-free AgAuSe colloidal quantum dots. *J. Mater. Chem. C* **2022**, *10*, 1097–1104. [[CrossRef](#)]
35. Kim, G.; Choi, D.; Eom, S.Y.; Song, H.; Jeong, K.S. Extended short-wavelength infrared photoluminescence and photocurrent of nonstoichiometric silver telluride colloidal nanocrystals. *Nano Lett.* **2021**, *21*, 8073–8079. [[CrossRef](#)]
36. Yan, S.G.; Deng, D.Y.; Li, L.; Chen, Y.C.; Song, H.J.; Lv, Y. Glutathione modified Ag₂Te nanoparticles as a resonance Rayleigh scattering sensor for highly sensitive and selective determination of cytochrome C. *Sens. Actuators B Chem.* **2016**, *228*, 458–464. [[CrossRef](#)]
37. Chang, P.J.; Cheng, H.Y.; Zhao, F.Y. Photocatalytic reduction of aromatic nitro compounds with Ag/Ag_xS composites under visible light irradiation. *J. Phys. Chem. C* **2021**, *125*, 26021–26030. [[CrossRef](#)]
38. Dinda, D.; Ahmed, M.E.; Mandal, S.; Mondal, B.; Saha, S.K. Amorphous molybdenum sulfide quantum dots: An efficient hydrogen evolution electrocatalyst in neutral medium. *J. Mater. Chem. A* **2016**, *4*, 15486–15493. [[CrossRef](#)]

39. Denton, A.R.; Ashcroft, N.W. VEGARD LAW. *Phys. Rev. A* **1991**, *43*, 3161–3164. [[CrossRef](#)] [[PubMed](#)]
40. Kershaw, S.V.; Susha, A.S.; Rogach, A.L. Narrow bandgap colloidal metal chalcogenide quantum dots: Synthetic methods, heterostructures, assemblies, electronic and infrared optical properties. *Chem. Soc. Rev.* **2013**, *42*, 3033–3087. [[CrossRef](#)]
41. Du, Y.P.; Xu, B.; Fu, T.; Cai, M.; Li, F.; Zhang, Y.; Wang, Q.B. Near-infrared photoluminescent Ag₂S quantum dots from a single source precursor. *J. Am. Chem. Soc.* **2010**, *132*, 1470–1471. [[CrossRef](#)] [[PubMed](#)]
42. Zhang, Y.; Zhang, Y.J.; Hong, G.S.; He, W.; Zhou, K.; Yang, K.; Li, F.; Chen, G.C.; Liu, Z.; Dai, H.J.; et al. Biodistribution, pharmacokinetics and toxicology of Ag₂S near-infrared quantum dots in mice. *Biomaterials* **2013**, *34*, 3639–3646. [[CrossRef](#)] [[PubMed](#)]
43. Chen, C.; He, X.W.; Gao, L.; Ma, N. Cation exchange-based facile aqueous synthesis of small, stable, and nontoxic near-infrared Ag₂Te/ZnS core/shell quantum dots emitting in the second biological window. *ACS Appl. Mater. Interfaces* **2013**, *5*, 1149–1155. [[CrossRef](#)]
44. Jeon, J.W.; Jeon, D.W.; Sahoo, T.; Kim, M.; Baek, J.H.; Hoffman, J.L.; Kim, N.S.; Lee, I.H. Effect of annealing temperature on optical band-gap of amorphous indium zinc oxide film. *J. Alloys Compd.* **2011**, *509*, 10062–10065. [[CrossRef](#)]
45. Wang, Z.; Gu, Y.J.; Li, X.M.; Liu, Y.; Liu, F.H.; Wu, W.P. Recent progress of quantum dot infrared photodetectors. *Adv. Opt. Mater.* **2023**, *11*, 2300970. [[CrossRef](#)]
46. Guo, D.Y.; Wu, Z.P.; An, Y.H.; Guo, X.C.; Chu, X.L.; Sun, C.L.; Li, L.H.; Li, P.G.; Tang, W.H. Oxygen vacancy tuned Ohmic-Schottky conversion for enhanced performance in β -Ga₂O₃ solar-blind ultraviolet photodetectors. *Appl. Phys. Lett.* **2014**, *105*, 023507. [[CrossRef](#)]

Disclaimer/Publisher's Note: The statements, opinions and data contained in all publications are solely those of the individual author(s) and contributor(s) and not of MDPI and/or the editor(s). MDPI and/or the editor(s) disclaim responsibility for any injury to people or property resulting from any ideas, methods, instructions or products referred to in the content.